ISSN (Print) 1226-1750
ISSN (Online) 2233-6656
Journal of Magnetics 26(1), 101-110 (2021) https://doi.org/10.4283/JMAG.2021.26.1.101

Array Sensing Using Differential Magnetic Field Method for Electrode Tip Position of Submerged Arc Furnaces

Wei Ling Liu[1], Xiao Hong Han[1], Ling Zhen Yang[2]*, and Xiao Ming Chang[3]

[1]*College of Data Science, Taiyuan University of Technology, No. 79 Yingze West Street, Taiyuan 030024, Shanxi, PR China*
[2]*College of Physics and Optoelectronics, Taiyuan University of Technology, No.79 Yingze West Street, Taiyuan 030024, Shanxi, PR China*
[3]*College of Information and Computer Science, Taiyuan University of Technology, No.79 Yingze West Street, Taiyuan 030024, Shanxi, PR China*

(Received 19 December 2020, Received in final form 25 March 2021, Accepted 25 March 2021)

This paper proposes an array sensing methodology with differential magnetic field for electrode tip position in different smelting periods for high-power submerged arc furnace (SAF). According to the difference of magnetic field distribution between the electrode zone and the arc zone, the magnetic field radiation model of SAF is constructed, and the array detection system of differential magnetic field is designed and developed. The magnetic field distribution information of electrode zone and arc zone is collected on the electrode line of SAF. The test curve appears to be consistent with theoretical simulation result which indicates that the peak point of the magnetic field distribution curve on the electrode line is near the electrode tip of SAF. Compared with the single-point detection method of differential magnetic field, this method shows higher performance in accuracy and real-time, which should make an important contribution to the measurement of electrode tip position.

Keywords : submerged arc furnace, electrode tip position, differential magnetic field, array sensing

1. Introduction

Submerged arc furnace (SAF) is an industrial electric furnace which can smelt ores and extract useful metals by electric arc discharge. The electric arc occurs between the furnace burden and the tip of electrodes which are the pivotal components that inject large current into the furnace to perform arc smelting [1]. SAF is an energy-consuming equipment in the industrial sector, and the ton consumption of national standard is 4200-4400 KWh/t [2]. A huge amount of energy needs to be transported to the furnace in a short time to maintain the redox reaction. The output voltage of the SAF transformer is low, which is generally lower than the mains voltage. In this way, the output current of the transformer should be very large to meet the power of the furnace. Under the condition of high power and high current, the unbalance of the three-phase load of the SAF affects the economic parameters such as smelting energy consumption and ore consumption, which is a great challenge to the production technical index and economic benefit of the ferroalloy smelter. The power balances control is the best way to the smelting of SAF, and the balance of three-phase power pool is mediated by elevating electrodes [3, 4]. Because the heat in the reaction area is provided by the electric arc heat produced by the electrode tip, the consistent position of the three electrode tips is the key factor of three-phase load balancing. Consequently, the detection of the electrode tip position is of great significance to production of SAF. The temperature in the crucible area is as high as 2000 °C-2500 °C, and the temperature within the crucible wall and outside the crucible are about 1900 °C and 1700 °C, respectively, so the detection for smelting parameters is very difficult in the environment of high temperature [5]. Up to now, several methods are proposed to measure electrode tip position. Tang *et al.* [6] presented an approach to calculate the working length of the electrode by the variables such as self-weight of the electrode, lifting displacement and slipping length of the electrode and so on, in which the measurement model is established under the assumption that the electrodes are regular and uniform, so the measurement deviation is large, and this

*Corresponding author: Tel: 132-3369-7523
Fax: 0351-6014033, e-mail: 644855751@qq.com

method requires the installation of a complex set of equipment on the furnace, which is not conducive to the production of ferroalloy smelters in the later stage. Bai *et al.* [7, 8] proposed a way in which the photoelectric and position sensors can be used to design an online detection system for the relative position of electrodes. The measurement error of this method is small, but the displacement sensor is expensive, and the high temperature environment of SAF makes the installation of the photoelectric sensor inconvenient. Liu *et al.* [9] proposed the magnetic field array sensing, however, this method needs to identify the characteristics of the electrode tip correctly for the high-power SAF, which is very difficult. Liu *et al.* [10] presents the method of differential single-point magnetic field detection, which needs the stable furnace condition. However, the smelting of SAF is a very complex process which contains physical and chemical reaction and heat exchange in real application. Thus, the differential single-point magnetic field detection has the large error when the furnace condition fluctuates greatly.

In view of the shortcomings of the above detection methods, we analysis the relationship among the external magnetic field, the electrode current and arc current in the furnace based on the electromagnetic theory. The array sensing is proposed to detect the electrode tip position using differential magnetic field and the effectiveness is verified by the theoretical model and simulation. The preliminary experiment shows that the proposed method has the higher measurement accuracy than the single-point detection of differential magnetic field, and can be used to determine electrode tip position.

The paper is organized as follows: The magnetic field detection model is introduced in section 2. Section 3 describes the design and implementation of the differential magnetic array. The verification of detection scheme for differential magnetic array sensing is presented in Section 4, and conclusions are given in Section 5.

2. Theory Background

2.1. Magnetic field radiation model

The hearth structure [11-13] of SAF is presented in Fig. 1.

The electric arc is generated between the electrode tip and the molten bath shown in Fig. 1. The molten alloys gather in the molten bath and the liquid level is on the top of the molten bath surface.

The large currents flow into the furnace through the electrodes, and the circuit can be treated as star circuit loop or triangle circuit loop [14, 15]. These two types of loops can be equivalently transformed in the sense of

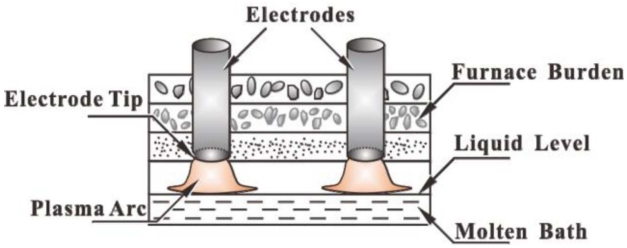

Fig. 1. (Color online) The hearth structure of SAF.

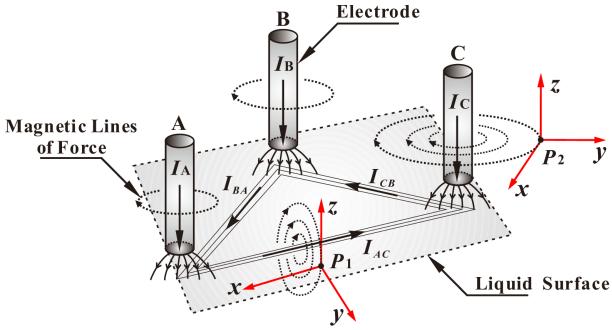

Fig. 2. (Color online) The magnetic field radiation model of SAF.

electromagnetic. So the triangle loop is used to analyze the circuit model. Based on the electromagnetism, magnetic field radiation model of SAF shown in Fig. 2 [16] is established.

As can be seen from the Fig. 2, I_A, I_B, and I_C are the currents of electrode A, B, and C, respectively, and I_{AC}, I_{CB}, and I_{BA} are the currents in the molten bath. Currents flow into the furnace along each electrode and form a triangle circuit loop near the liquid surface. I_{AC} is the molten bath current parallel to the x-axis at point P_1; I_C is the electrode current parallel to the z-axis at point P_2. The concepts of electrode line and perpendicular bisector shown in Fig. 3 are defined.

Fig. 3 provides a vertical view of SAF. On the plane parallel to the molten bath surface, a regular triangle is generated by connecting three vertex electrodes, and the

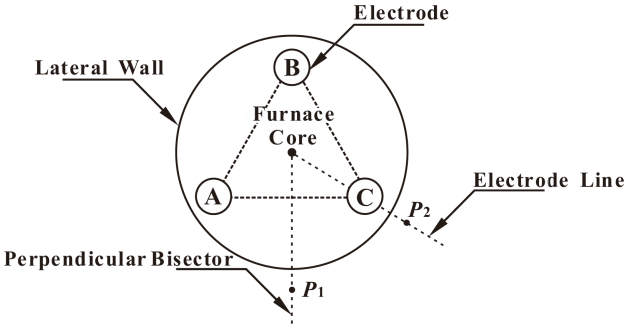

Fig. 3. Vertical view of SAF.

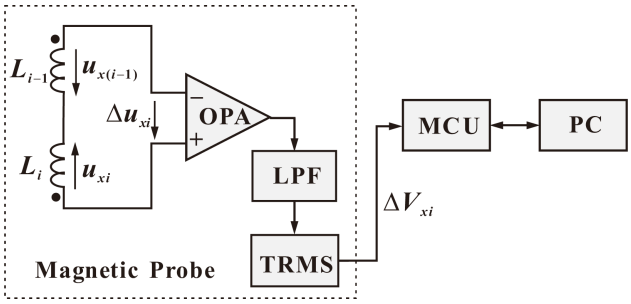

Fig. 4. The single-point detection system of differential magnetic field.

core of SAF is the center of the triangle. The vertical line of each edge of the regular triangle is called by perpendicular bisector [16], and the line connecting the electrode and the furnace core is termed as electrode line [16].

2.2. Differential single-point detection [10]

The single-point detection system of differential magnetic field is composed of a 3D probe, a microcontroller and a PC, as shown in Fig. 4.

In Fig. 4, the MCU collects the magnetic field intensity after receiving the orders given by the PC, and sends the collected information back to the PC. The probe is composed of two opposite polarity coils which detect magnetic field at different spatial positions. The difference value between the outputs of the two coils is converted into the output ΔV_{xi} by the OPA circuit and LPF circuit, and then by the TRMS conversion circuit.

The differential single-point magnetic field detection way, which has been discussed in Ref. [10], can extract the characteristics and detect the electrode tip position. The detection model is shown in Fig. 5.

In Fig. 5, the distance between the origin o and the sensor S_1 is 10 cm, and the electrode tip can be covered

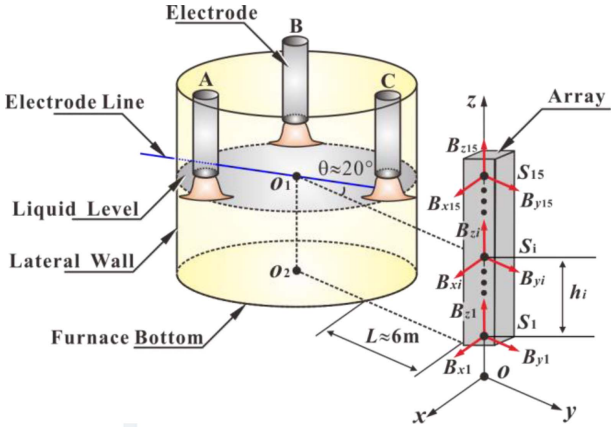

Fig. 5. (Color online) The schematic diagram of measuring in real industrial field.

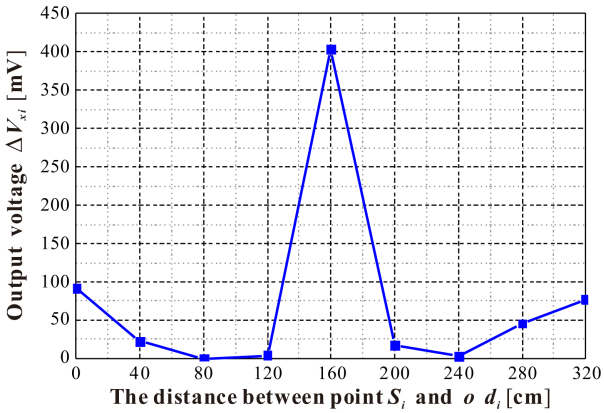

Fig. 6. (Color online) The testing results of the single-point detection of differential magnetic field.

by the measurement range. According to the detection model, the real measurements on the SAF (33000 KVA) are achieved at a metallurgical company in Yinchuan city in China. The mean of multiple measuring results in industrial field is shown in Fig. 6.

From Fig. 6 we can see that the peak point appears at the test point d_i = 160 cm. Since the distance between the two coils of the system is 40 cm, we can conclude that the region of the electrode tip is in the range of 140 cm ≤ d_i ≤ 180 cm, which is in accordance with the field situation of SAF. Therefore, the characteristics distribution of the magnetic field of SAF can be reflected and the electrode tip position can be obtained by the single-point detection of differential magnetic field.

The measurements with the single-point detection of differential magnetic field were also carried out in four different smelting periods of SAF, and the measurement interval is about 10 minutes. The results are shown in Fig. 7.

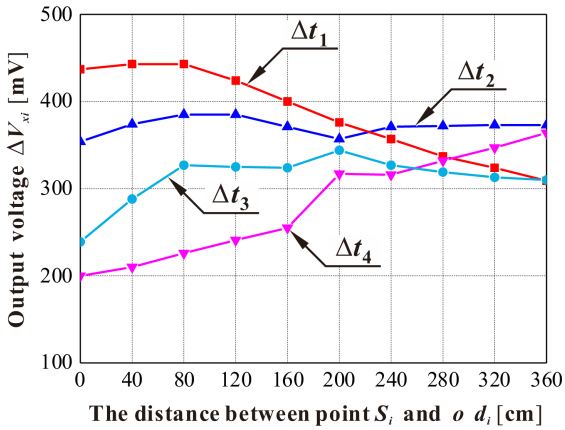

Fig. 7. (Color online) The testing results in different smelting periods.

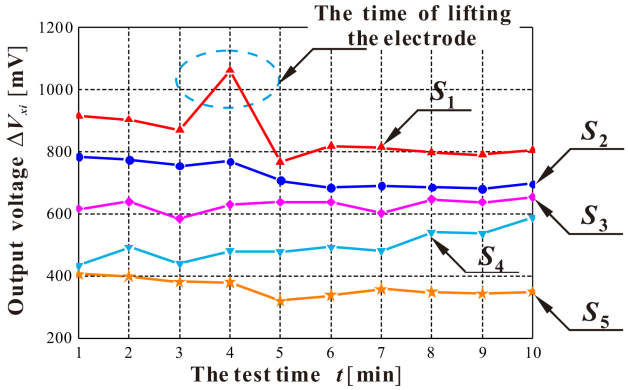

Fig. 8. (Color online) The variation of magnetic field intensity with time at five spatial positions.

By analysis of the curve in Fig. 7, it is difficult to capture the characteristic value, and the output value of the magnetic field detection system fluctuates greatly at different moments in the same position, which is caused by the fluctuation of the furnace condition during the smelting process of SAF.

To solve the above problems, we tested the furnace conditions of five points at different times where the spatial positions of the five test points remained unchanged. The test curve is shown in Fig. 8.

From Fig. 8 we can see that the magnetic field intensity of the five test points varies in the same position but at different time periods, which indicates that the furnace condition fluctuates frequently with the change of time. In addition, the magnetic field intensity of the five detection points varies at the same time as a result of the different spatial positions of the detection points or the sensitivity differences from the detection device. Besides, when the electrode is lifted about 3 cm, a peak point appears in the magnetic field intensity curve, which shows that the lift of the electrode has a great influence on the current fluctuation.

In order to further observe the variation of magnetic induction intensity with time at a certain point, a 16-hour experiment was carried out on the site of SAF. Two sensors were located below the outlet of the furnace, and the measured curve is shown in Fig. 9.

In Fig. 9 the on-site smelting cycle of SAF is about 4 hours. In the same smelting cycle, the electrode tip position is changing at any time as a consequence of the consumption of electrodes, the loss of the electrode tip, or the lift of the electrodes. Consequently, the electrode current and arc current are also changing, which is a challenge for the detection system in real-time. However, for any system in which critical real- time performance is demanded, the delay time caused by information trans-

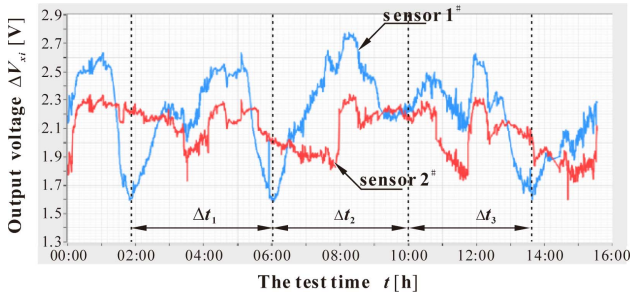

Fig. 9. (Color online) The variation of magnetic field strength with time over a period of 16 hours at a certain point.

mission is inevitable and can't be ignored [17]. For the system of single-point detection of differential magnetic field, we define the single sampling and processing time as T_{SP} that can be expressed as Eq. (1).

$$T_{SP} = \sum_{i=1}^{5} T_{Si} \tag{1}$$

In Eq. (1), T_{S1}, T_{S2}, T_{S3}, T_{S4}, T_{S5} are the time of sensor collection, signal amplification, low-pass filtering, TRMS conversion and MCU processing, respectively. In the practical engineering application, T_{S1}, T_{S2}, T_{S3} and T_{S5} are all in the level of milliseconds. However, TRMS conversion obeys the principle of circuit integral, and the higher the expected precision is, the longer the processing time that TRMS conversion takes will be. In general terms, the time, for the TRMS circuit converting to stable states, T_{S4}, is nearly equal to $T_{S4} \approx 3$~5 s. Only taking the TRMS conversion time T_{S4} into account, the single sampling and processing time T_{SP} can be expressed by the following equation:

$$T_{SP} \approx T_{S4} \approx 3 \sim 5\text{s} \tag{2}$$

In the single-point detection way of differential magnetic field, the probe needs to be moved to the next the detection point after collecting the data at a point. To sample N points, the time T_{NS} is presented as Eq. (3).

$$T_{NS} \approx N \times T_{SP} + (N-1) \times T_{MOV} \tag{3}$$

where N is the number of sampling points. T_{MOV} is the moving time between the adjacent points. In the practical engineering fields, $T_{MOV} \geq 30$ s.

As previously stated, the minimum values of the sampling and processing time T_{SP} and the moving time T_{MOV} are approximately equal to $T_{SP\,(\min)} \approx 3$s and $T_{MOV(\min)} \approx 30$s, respectively. Take these two parameters mentioned above into Eq. (3), we can get the minimum value of the time T_{NS} which is given as Eq. (4).

$$T_{NS(\min)} \approx 33N - 30 \tag{4}$$

We can see clearly from Eq. (4) that the collecting time T_{NS} increases with the number of sampling points. When the total measurement length and the sampling spatial distance are 320 cm and 10 cm respectively, the number of sampling points is 32. According to Eq. (4), the collecting time T_{NS} is at least 17 minutes and 6 seconds, during which the furnace condition may have changed greatly, so the single-point detection way of differential magnetic field can not truly reflect the furnace condition. In addition, there still exist the measurement errors, and the factors causing errors mainly include the following aspects:

(1) Owing to the trembling of the mechanical equipment, it is difficult to keep the measurement baselines and datum planes consistent in the process of moving.

(2) Because of the movement of mechanical equipment, it is difficult to make the spatial sampling interval uniform at different positions.

According to the above analysis, the single-point detection system of differential magnetic field is difficult to satisfy the measurement demand in the real industrial field.

2.3. Modelling the array sensing detection of differential magnetic field

As previously stated, the single-point detection method of differential magnetic field has several problems in measurement accuracy. To solve the problems, we propose an array sensing detection method of differential magnetic field based on the principle of datum plane unity in theory of instrument precision [18]. The system composition of the proposed method is shown in Fig. 10.

In Fig. 10, the magnetic array is composed of N probes arranged in a linear and uniform way and every probe is equipped with a sub-microcontroller (S_MCU). After the main-microcontroller (M_MCU) receives the commands from PC, N S_MCUs are triggered to collect the data of magnetic field simultaneously, and then send the information back to PC.

From Fig. 10, we can see that there is no moving time

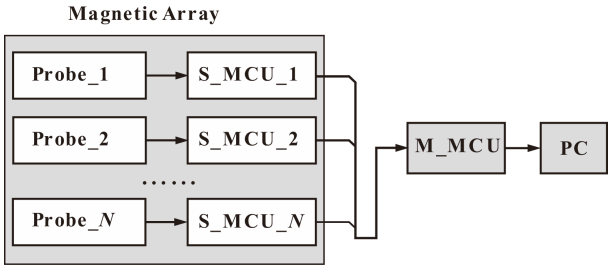

Fig. 10. The system composition of the array sensing detection of differential magnetic field.

in the array sensing detection way. As a result, when N S_MCUs gather the data simultaneously, the delay time T_{NA} equals to the single sampling and processing time, or T_{SP}, as shown in Eq. (5).

$$T_{NA} \approx T_{SP} \tag{5}$$

The acquisition time of the array sensing system of differential magnetic field is equal to $T_{NA} \approx 3$s from Eq. (5) and it is unrelated to the sampling points number.

Based on the above analysis, we conclude that the array sensing detection of differential magnetic field simplifies the design of mechanical connection structure and the maintenance of equipment in later periods. This method makes spatial sampling interval uniform and keeps the measuring baselines and datum planes consistent, thereby improving the testing precision and collection efficiency greatly.

3. Design and Implementation

3.1. Distribution characteristics of magnetic field

3.1.1. Current distribution in electrode zone and arc zone

The electrode top is assumed to be the origin o, and we take p points vertically down as the test points (S_1, …, S_m, …, S_n, …, S_p), among which the point S_m is located at the electrode tip, and the point S_n is at the liquid level, $m < n < p$, and the distances between the point o and these test points are (d_1, …, d_m, …, d_n, …, d_p), respectively. The distribution model of electrode current, arc current and the current in molten liquid are shown in Fig. 11 [19, 20].

In Fig. 11 the current is uniformly distributed in the electrode above the point S_m in the range of $d_1 \le d_i \le d_m$. However, owing to the changing medium between the detected point S_m and S_n ($d_m \le d_i \le d_n$) in the arc zone

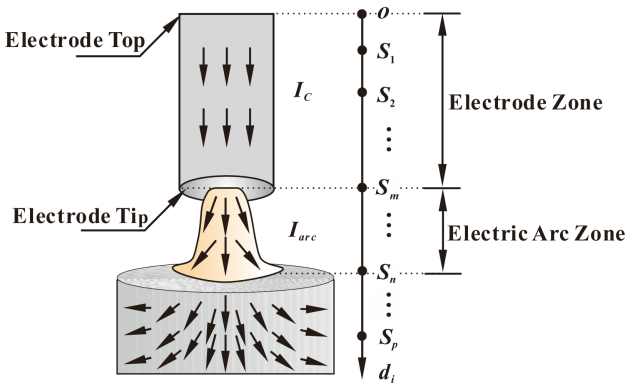

Fig. 11. (Color online) The current distribution of electrode, electric arc and molten bath.

[21], the direction of the arc current appears randomness and inhomogeneity.

3.1.2. Magnetic field distribution in electrode zone

The electrode is equivalent to a current-carrying straight wire A_1A_2 with the finite length. The length and average current at z-axis direction are L_C and I_C, respectively. The line S_iM is the vertical line of electrode A_1A_2, and the length of S_iM is r, namely the distance between the test point and the center of electrode column, as shown in Fig. 12.

Based on the Biot-Savart law [22], the magnetic induction intensity dB which is generated by any current element Idl is in the same direction and is parallel to the x-axis. Therefore, in order to calculate the total magnetic induction intensity B_x at the point S_i, we only need to compute the algebraic sum of dB_x. For the electrode A_1A_2, the total magnetic induction intensity B_x at the test point S_i can be described as Eq. (6).

$$B_x = \int_{A_1}^{A_2} dB_x = \frac{\mu_0}{4\pi}\int_{A_1}^{A_2} \frac{I_C dl \sin\theta}{r_0^2} \tag{6}$$

where I_C is the electrode current. r_0 is the radius vector from the current element Idl to the test point S_i. r_1 is the radius vector from the starting point A_1 of the straight wire carrying current I_C to the field point S_i. r_2 is the radius vector from the end point A_2 of the straight wire carrying current I_C to the field point S_i. q_1 is the angle between the radius vector r_1 and the current element located at the starting point A_1 of the straight wire. q_2 is the angle between the radius vector r_2 and the current element located at the end point A_2 of the straight wire.

l is assumed as the distance from the current element Idl to the foot point M. It can be seen from Fig. 12:

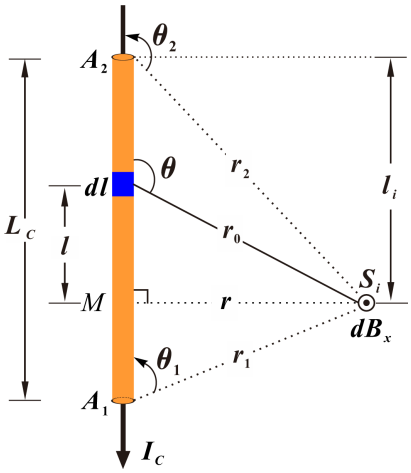

Fig. 12. (Color online) The magnetic induction intensity of the measuring point S_i in electrode zone.

$$\begin{cases} l = r_0\cos(\pi-\theta) = -r_0\cos\theta \\ r = r_0\sin(\pi-\theta) = r_0\sin\theta \end{cases} \tag{7}$$

in which r is the distance from the detection point S_i to the vertical line S_iM.

According to Eq. (7) the distance l from the current element Idl to the foot point M can be modified as the following equation:

$$l = -r\cot\theta \tag{8}$$

Take the derivative with respect to l, and then dl that is the differential calculus of l is given as Eq. (9).

$$dl = \frac{rd\theta}{\sin^2\theta} \tag{9}$$

Replace the integral variable l in the formula above with θ, so the total magnetic induction intensity B_x is presented as Eq. (10).

$$\begin{aligned} B_x &= \frac{\mu_0}{4\pi}\int_{\theta_1}^{\theta_2} I_C \frac{\sin\theta}{r} d\theta \\ &= \frac{\mu_0 I_C}{4\pi r}(\cos\theta_1 - \cos\theta_2) \end{aligned} \tag{10}$$

From Fig. 12, the expressions of $\cos\theta_1$ and $\cos\theta_2$ are described in Eq. (11).

$$\begin{cases} \cos\theta_1 = \dfrac{L_C - l_i}{\sqrt{(L_C - l_i)^2 + r^2}} \\ \cos\theta_2 = -\dfrac{l_i}{\sqrt{l_i^2 + r^2}} \end{cases} \tag{11}$$

where L_C is the total length of electrode, or the distance between the points A_1 and A_2 of the electrode; l_i is the distance between the test point S_i and the point A_2 which is located at the electrode top.

Take Eq. (11) into Eq. (10), the total magnetic induction intensity B_x at the test point S_i is expressed as the following equation:

$$B_x \approx \frac{\mu_0 I_C}{4\pi r}\left(\frac{l_i}{C} - \frac{A}{B}\right) \tag{12}$$

A, B and C in Eq. (12) are respectively expressed as follows:

$$\begin{aligned} &A = l_i - L_C; \\ &B = \sqrt{(L_C - l_i)^2 + r^2}; \\ &C = \sqrt{l_i^2 + r^2}. \end{aligned}$$

3.1.3. Magnetic field distribution in arc zone

The electric arc is equivalent to a current-carrying

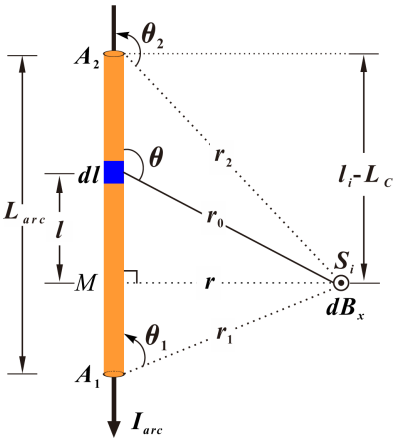

Fig. 13. (Color online) The magnetic induction intensity of the measuring point S_i in electric arc zone.

straight wire A_1A_2 with the finite length. The length and average current at z-axis direction are L_{arc} and I_{arc}, respectively. The line S_iM is the vertical line of electric arc A_1A_2, and the length of S_iM is r which is the distance between the test point and the center of arc column, as shown in Fig. 13.

Similarly, for the finite electric arc A_1A_2, the total magnetic induction intensity B_x at the test point S_i can be described as Eq. (13).

$$\begin{aligned} B_x &= \frac{\mu_0}{4\pi}\int_{\theta_1}^{\theta_2} I_{arc}\frac{\sin\theta}{r}d\theta \\ &= \frac{\mu_0 I_{arc}}{4\pi r}\left(\cos\theta_1 - \cos\theta_2\right) \end{aligned} \tag{13}$$

where I_{arc} is the current of the electric arc. r is the distance from the detection point S_i to the vertical line S_iM of the electric arc A_1A_2.

The expressions of $\cos\theta_1$ and $\cos\theta_2$ can be obtained from Fig. 13, as shown in Eq. (14).

$$\begin{cases} \cos\theta_1 = \dfrac{L_{arc} - l_i + L_C}{\sqrt{(L_{arc} - l_i + L_C)^2 + r^2}} \\ \cos\theta_2 = -\dfrac{l_i - L_C}{\sqrt{(l_i - L_C)^2 + r^2}} \end{cases} \tag{14}$$

where L_{arc} is the distance between the extreme points A_1 and A_2 of the electric arc.

Substitute Eq. (14) into Eq. (13), the total magnetic induction intensity B_x at the test point S_i is expressed as the following equation:

$$B_x \approx \frac{\mu_0 I_{arc}}{4\pi r}\left(\frac{D}{E} + \frac{A}{B}\right) \tag{15}$$

D and E in Eq. (19) are respectively expressed as follows:

$$D = L_{arc} - l_i + L_C;$$
$$E = \sqrt{(L_{arc} - l_i + L_C)^2 + r^2}.$$

3.1.4. Magnetic field distribution in electrode line

As explained above, B_x is the algebraic sum of the magnetic induction intensity in the arc zone current and the electrode zone current, as shown in Eq. (16).

$$B_x \approx \frac{\mu_0 I_C}{4\pi r}\left(\frac{l_i}{C} - \frac{A}{B}\right) + \frac{\mu_0 I_{arc}}{4\pi r}\left(\frac{D}{E} + \frac{A}{B}\right) \tag{16}$$

3.2. Output characteristics of differential magnetic array sensor

The output characteristics of differential magnetic field array is discussed. l_i and l_{i+1} are the height of the detection point S_i and S_{i+1}, and B_{xi} and $B_{x(i+1)}$ are the magnetic flux density of S_i and S_{i+1}, respectively. Set $\Delta l = l_{(i+1)} - l_i$, the variation of D$B_x$ between adjacent points is defined as $\Delta B_x = B_{x(i+1)} - B_x$. The distribution characteristic of B_x and the relation between ΔB_x and Δl are given in Fig. 14.

In Fig. 14, the tangent at detection point S_i is S_iT. Using the method of local linearization of nonlinear functions in differential calculus [23], the curve segment S_iS_{i+1} near the point S_i can be substituted by the tangent section S_iP. In other words, dB_x is approximately equal to ΔB_x. Therefore, when the derivative $\left|B_x'(l_i)\right| \neq 0$ at certain point and Δl is relatively small, the output of the array of the differential magnetic field is presented in Eq. (17).

$$\left|\Delta B_x\right| \approx dB_x = \left|B_x'(l_i)\right|\Delta l \tag{17}$$

According to Eq. (17), the output characteristic of the differential array is the variation tendency of $\left|B_x'(l_i)\right|$. Thus, we can differentiate the formula for B_x to get the change rate of the total magnetic induction intensity B_x in the electrode line, as shown in Eq. (18).

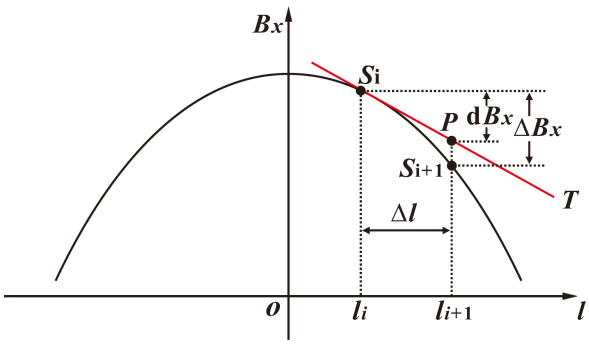

Fig. 14. (Color online) The distribution characteristic of B_x and the relation between ΔB_x and Δl.

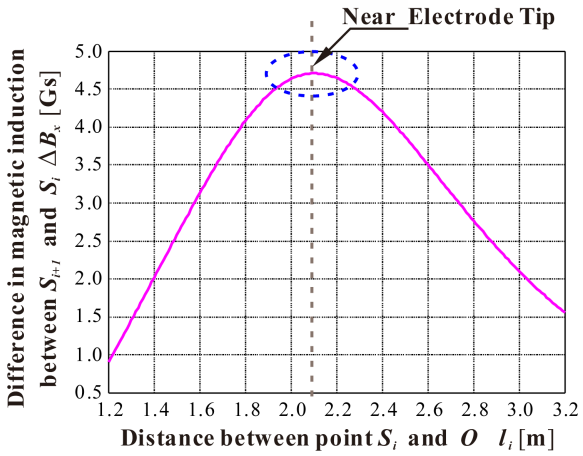

Fig. 15. (Color online) The simulation results of the output ΔB_x of the differential magnetic sensor array.

$$\left|B_x^{'}(l_i)\right| = \left| \begin{array}{l} \dfrac{\mu_0 I_C}{4\pi r}\left(\dfrac{A^2}{B^3} - \dfrac{1}{B} + \dfrac{1}{C} - \dfrac{l_i^2}{C^3}\right) + \\ \dfrac{\mu_0 I_{arc}}{4\pi r}\left(\dfrac{D^2}{E^3} - \dfrac{1}{E} + \dfrac{1}{B} - \dfrac{A^2}{B^3}\right) \end{array} \right| \tag{18}$$

Considering with the actual circumstances in the field of SAF, take $\mu_0 = 4\pi \times 10^{-7}$ H/m, $r = 1$ m, $\Delta l = 0.1$ m, $I_C \approx 54.414$ kA [2], $I_{arc} \approx 10$ kA [24, 25], $L_{\text{arc}} \approx 0.5$ m [12], $L_C = 2$ m. On the basis of Eq. (18), the Maple software is used for simulation of the output ΔB_x of the differential magnetic array. The simulation results are set out in Fig. 15.

The following conclusions can be drawn from Fig. 15.

(1) The output ΔB_x from the differential magnetic field array appears a trend of normal distribution on the electrode line.

(2) The output value of the array rises to the peak point at $l_i \approx 2.095$ m, and begins to fall within the range of $l_i \geq 2.1$ m.

(3) As the total length of the electrode L_C is equal to 2 m, it can be concluded from the simulation results that the peak point among the output values of the array is near the electrode tip position.

4. Verification of Detection Scheme

4.1. Physical structure of differential magnetic field array

The differential magnetic field array is equipped with a differential array unit, a signal processing circuit board, a power supply, and a wireless module. The internal structure of the differential array unit is shown in Fig. 16.

In Fig. 16, the coil spacing is 5cm. The coils are divided into two groups: the upper coil group and the lower coil group. Each group is composed of 10 coils. Fig. 17 presents the probe structure of differential array.

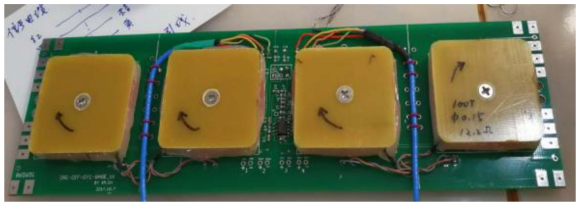

Fig. 16. (Color online) The internal structure of the differential array unit.

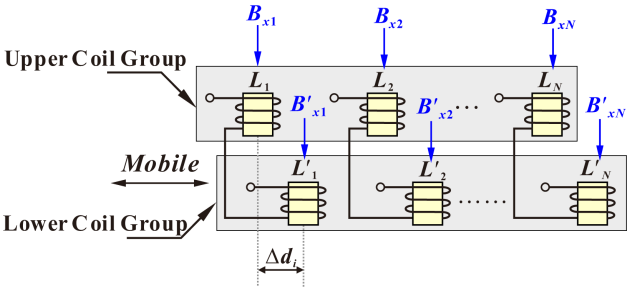

Fig. 17. (Color online) Design of the probe structure of the differential array.

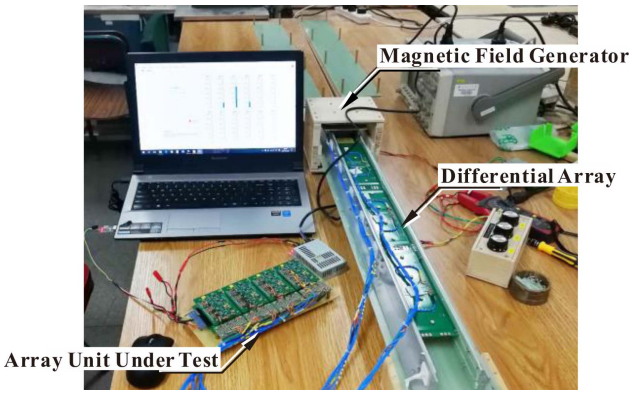

Fig. 18. (Color online) Debugging scene of differential magnetic field array system.

As can be seen from Fig. 17, the outputs of the upper and lower coils are differentiated in sequence. The position of the upper coils remains unchanged, while the lower coils can be flexibly adjusted. Therefore, the distance Δd between the two differential coils is variable. Fig. 18 is the debugging scene of differential magnetic field array system.

The differential magnetic field array in Fig. 18 consists of 10 channels. The sensitivity of each channel is tested and their consistency is verified.

4.2. Verification by field tests

The measurements in real scene are performed on the

Fig. 19. (Color online) The experimental scene in the industrial field of SAF.

33000KVA SAF at a metallurgical company of Yinchuan city in China. The test site is chosen at the electrode line and is about 1m away from the lateral wall through a number of trials. Fig. 19 provides the experimental scene in the industrial field of SAF.

The height of the furnace in Fig. 19 is 5.6 m. The differential magnetic array is vertically placed on the lifting and lowering device. During the process of the test, the array is moved up and down, and its moving range covers the electric tip. The electrode top is set as the coordinate origin *O*.

4.3. Test result and analysis

The experimental results show that the most ideal sampling result can be gotten when the sampling interval is 10 cm and the distance between the two coils of the system is 3 cm. Especially, the characteristic of the electrode tip position is relatively obvious when the detection point is within the range of 1.1 m-2.2 m. The average values of multiple sampling points are computed. The test results are presented in Fig. 20.

As can be seen from Fig. 20, the peak point before and after moving the array are 1.565 m and 1.665 m, respectively. The horizontal ordinate of the cross point between the two curves lies at 1.605 m. It can be inferred that the electrode tip position is located near 1.605 m. Therefore, when the position of the differential magnetic array is changed, the initial position of the sampling point is placed at 1.2 m and the sampling interval remains 10 cm. The test curve is provided in Fig. 21.

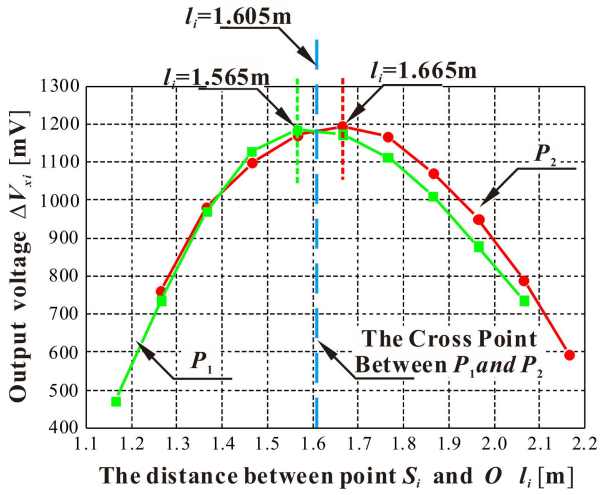

Fig. 20. (Color online) Measured curves after the moving the array.

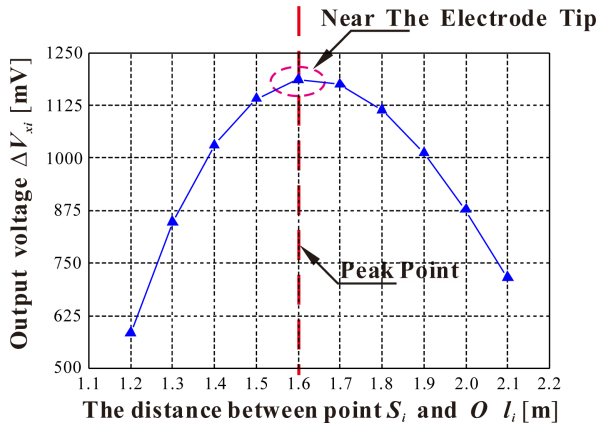

Fig. 21. (Color online) Analysis on measured results of SAF.

From the graph above we can see that the peak point appears at the test point l_i = 1.6 m. For the distance between the two coils of the system is 3cm, it can be concluded that the electrode tip position ranges from 1.45 m to 1.75 m, which is in accordance with the simulation results in Fig. 15.

5. Conclusions

In this paper, an array sensing technique with differential magnetic field is proposed to obtain the electrode tip position. Compared with the single-point detection of differential magnetic field, the proposed method is greatly improved in the performance of efficiency, accuracy, and real-time, which makes the later maintenance more convenient. Moreover, theoretical analysis and practical measurements confirm that when the sampling interval is 10 cm and the distance between the two coils of the array is

3 cm, the most ideal result can be obtained, thus the characteristic value can be extracted and then the electrode tip position can be achieved.

Acknowledgements

This research has been supported by National Natural Science Foundation of China under Grant (61975141 and 61575137), Natural Science Foundation of Shanxi Province of China under Grant (201801D121136), and Shanxi Scholarship Council of China under Grant (HGKY2019024).

References

[1] M. Moghadasian and E. Alenasser, J. Electromagn. Anal. Appl. **3**, 47 (2011).
[2] K. F. Hu, Ms. D. Thesis, Central. South. Univ, China (2013).
[3] A. C. Mulholland, P. J. Breretonstiles, and C. J. Hockaday, J. S. Afr. I. Min. Metall. **109**, 601 (2009).
[4] N. N. Zhang, Z. J. Wang, and D. J. Zhang, IEEE. Comput. Mechatr. Contr. Electr. Eng. **3**, 108 (2010).
[5] G. Z. Zhang, W. C. Duan, B. B. Dong, and G. H. Han, China. Metall. **27**, 68 (2017).
[6] C. X. Tang, C. H. Yang, P. Li, and X. X. Lei, J. Changsha. Social. Work. Col. **20**, 123 (2013).
[7] Y. Bai, Q. Wang, F. R. Meng, and H. Y. Wang, J. Changchun. Univ. Tech. **33**, 383 (2012).
[8] Z. H. An, Ms. D. Thesis, Changchun. Univ. Tech, China (2010).
[9] W. L. Liu, X. H. Han, L. Z. Yang, and X. M. Chang, J. Magn. **21**, 322(2016).
[10] W. L. Liu, L. Z. Yang, and X. M. Chang, J. Magn. **25**, 78 (2020).
[11] S. J. Chu, S. L. Zeng, and Z. C. Huang, Ferro-Alloys. **2**, 13 (2009).
[12] S. J. Chu, X. E. Bao, and Z. S. Li, Ferro-Alloys. **3**, 22 (2013).
[13] A. S. Hauksdottir, T. Soderstrom, Y. P. Thorfinnsson, and A. Gestsson, IEEE. T. Contr. Syst. T. **3**, 377 (1996).
[14] Q. H. Xiao, Ferro-Alloys. **1**, 11 (1982).
[15] N. S. Zhang, Ferro-Alloys. **6**, 1 (1986).
[16] W. L. Liu and X. M. Chang, J. Magn. **21**, 204 (2016).
[17] C. C. Liu, Z. C. Jin, and C. J. Xu, J. Agricul. Machi. **25**, 28 (1994).
[18] H. Ma and J. B. Wang. Instrument Precision Theory, Beijing University of Aeronautics and Astronautics, Beijing (2014) pp 364-365.
[19] Z. K. Wang, T. W. Li, and B. K. Li, J. Mater. Metall. **12**, 177 (2013).
[20] J. Alexis, M. Ramirez, G. Trapaga, and P. Jonsson, ISIJ. International. **40**, 1089 (2000).
[21] Y. A. Tesfahunegn, T. Magnusson, M. Tangstad, and G. Saevarsdottir, J. S. Afr. I. Min. Metall. **118**, 595 (2018).
[22] O. J. P. Gonzalez, M. A. R. Argaez, and A. N. Conejo, ISIJ. International. **50**, 1 (2010).
[23] Department of Mathematics of Tongji University. Higher Mathematics, Higher Education, Beijing (2007) pp 113-123.
[24] F. Martell, M. Ramirez, A. Llamas, and O. Micheloud, ISIJ. International. **53**, 743 (2013).
[25] Z. Z. Mao, H. H. Shang, and J. Northeastern. Univ. **29**, 1398 (2008).